Tanzania Journal of Science 49(5): 1127-1137, 2023
ISSN 0856-1761, e-ISSN 2507-7961
© College of Natural and Applied Sciences, University of Dar es Salaam, 2023

Preparation of 2D Tungsten Diselenide (WSe_2) thin films by selenization of DC-sputtered W precursors

Lwitiko P. Mwakyusa
Department of Physics, Materials Science and Solar Energy Group, University of Dar es Salaam, P.O. Box 35063, Dar es Salaam, Tanzania
E-mail: mwakyusa.lwitiko@udsm.ac.tz
Received 16 Aug 2023, Revised 17 Nov 2023, Accepted Dec 2023, Published Jan 2024
https://dx.doi.org/10.4314/tjs.v49i5.15

Abstract

Two-dimensional layered transition metal dichalcogenides based on WSe_2 films demonstrated promising properties for nano-electronics and photovoltaic applications. In this work, WSe_2 films were prepared by selenization of DC-sputtered W precursors. The influence of the selenization temperature on the structural, morphology, and optical properties of the WSe_2 films was investigated. The selenization temperature was varied from 350 °C to 450 °C at the interval of 50 °C. Structural, morphology and optical properties of the WSe_2 were investigated using X-ray diffractometry (XRD), Atomic Force Microscope (AFM), and UV-VIS-NIR spectrophotometer, respectively. XRD analysis revealed that all WSe_2 were polycrystalline and exhibited the co-existence of *c*-axis perpendicular and parallel substrate texture. Samples selenized at 400 °C demonstrated strong $(00l)$ - types of crystal orientations – perpendicular *c*-axis substrate texture – dominated crystal growth. The AFM images further revealed the co-existence of parallel and perpendicular crystal orientations for samples selenized at 350 °C and 450 °C. Optical measurement showed that all WSe_2 samples were transparent and consisted of an excitonic peak at the wavelength of around 620 nm. The estimated bandgap values were in the range of 1.22 eV to 1.37 eV which is somewhat lower than expected – the presence of W_5O_{14} phases is suggested to be the main cause.

Keywords: Transition Metal Chalcogens, Two-dimensional layered WSe_2 films, crystal orientations, excitonic peak

Introduction

Transition Metal Dichalcogenides (TMDCs) materials are potential key semiconductor materials in the fabrication of the next optoelectronics devices, photovoltaic and Field-Effect Transistors (Bin Rafiq et al. 2020, Kadiwala et al. 2022). These materials are layered microstructures like graphite but possess optical bandgap and a substantial exciton binding energy (Brent et al. 2017, Villamayor et al. 2021). The layered microstructure comprised of the hexagonally-packed layer of transitional metal atoms sandwiched by two chalcogenides forming a triple layer of X-M-X (where X is chalcogen (Se or S) and M is transition metal) by a strong covalent bond (Bozheyev et al. 2017, Brent et al. 2017). The M-X layers are stacked over each other by weak van-der-Waals forces (Bozheyev et al. 2017, Rahman, 2022). Most of the TMDCs semiconductors such as MoX_2 demonstrated *n*-type electronic transport properties (Cheng et al. 2020). However, WX_2 was reported to have *p*-type semiconducting behaviour (Cheng et al. 2020, Lin et al. 2020). Surprisingly, these materials are less investigated compared to their counterpart MoX_2 – because it is more difficult to fabricate than MoX_2 (Salitra et al. 1994, Cheng et al. 2020). It has been documented that WX_2 is a highly textured film and grows in two forms i) *c*-axis parallel to the substrate and ii) *c*-axis

perpendicular to the substrate (Salitra et al. 1994). WX_2 with a *c*-axis parallel to the substrate texture demonstrated promising properties for photoelectrochemical hydrogen production (Genut et al. 1992, Morrish et al. 2014). On the other hand, WX_2 with a *c*-axis perpendicular texture can be used for photovoltaic applications (Morrish et al. 2014, Mao et al. 2018).

Considering the bandgap of WX_2 materials, it lies between 0 eV to 3 eV (Bin Rafiq et al. 2020, Zhang et al. 2020a) which can be tuned by thickness, defects, and dopants (Zhang et al. 2020a). Further, it exhibits a high absorption coefficient ($> 10^5$ cm^{-1}) (Bin Rafiq et al. 2020), making it an excellent candidate for thin film solar cell applications. It has been confirmed that the optical properties of WSe_2 films are thickness-dependent (Sierra-Castillo et al. 2020, Alzaid et al. 2022). For instance, the WSe_2 monolayer was demonstrated to have a higher bandgap which decreases with the number of layers (Sierra-Castillo et al. 2020, Villamayor et al. 2021). The optical bandgap of WS_2 films changes from a direct bandgap of 2 eV for monolayer films to an indirect bandgap of 1.3 eV for thicker films (Villamayor et al. 2021). An indirect bandgap in the range between 1.7 eV to 2.2 eV for 350 nm WS_2 films was reported by Bin Rafiq et al. (2020). A 75-nm WS_2 layer prepared by sulfurization of WO_3 films is reported to have an indirect bandgap of up to 1.4 eV (Morrish et al. 2014). A similar trend is expected for WSe_2 films. Several solar cells with *p*-type WX_2 absorber layers have been theoretically evaluated. WSe_2 with an efficiency of up to 22.24% utilizing Cu_2O hole transport layer could be theoretically demonstrated (Gautam et al. 2022). WSe_2-based solar cells with CuSCN hole transport with an efficiency of 24.2% could be realized (Haque et al. 2021). Theoretically, *p*-WSe_2 is a promising solar absorber layer for highly efficient devices.

Recently, the WSe_2 has been utilized as a buffer layer at the back electrode on the kesterite solar cells (Zhang et al. 2020b). Through this approach, devices with efficiencies of up to 5.45% were reported. Following these promising properties, indeed, WSe_2 film can be utilized as back contact in kesterite solar cells. With this regard, a bifacial thin film with WSe_2 back contact could be realized. Traditionally, ITO with a thickness of 150-200 nm and sheet resistance of up to 44 Ω/sq could be used as a transparent back contact for thin film solar cells (Bett et al. 2019). In this regard, understanding the structural and optical properties of WSe_2 with higher thicknesses is paramount. In line with this argument, the present work investigated the structural and optical properties of WSe_2 films with a thickness of around 150 nm. Preparation of WSe_2 films involves two steps, where i) W metal precursors were sputtered into the substrate and ii) followed by high-temperature selenization. The influence of selenization temperature on the structural, morphology, and optical properties of WSe_2 films was investigated and discussed.

Materials and Methods

WSe_2 films preparation

WSe_2 thin films were prepared by selenization of DC sputtered W metallic precursors. The precursors were deposited on Soda Lime Glass (SLG) substrates of dimensions 26 mm × 76 mm × 2 mm via DC magnetron sputtering in a BALZERS BAE 250 coating unit. The W precursors were sputtered from a 5.08 cm diameter × 0.635 cm thickness target with a purity of 99.99% supplied by Plasmaterials Inc. Before precursors deposition, the SLG substrates were cleaned as described by Mwakyusa et al. 2022 and then loaded in the sputtering chamber. The sputtering unit was evacuated to a base pressure of 10^{-6} mbar. The argon as a sputtering gas and working pressure was fixed to 50 sccm and 6.0×10^{-3} mbar, respectively. Using the sputtering power of 100 W, the W films were deposited for 8 min with the motivation of obtaining precursors with thicknesses of around 75 nm.

To obtain WSe_2 films, the metallic precursors were thermally annealed in a Se + N_2 atmosphere utilizing a semi-sealed graphite box containing 50 mg of Se pellets in a Rapid Thermal Processing (RTP-1000D4) tube furnace. Before annealing, the furnace was evacuated using a mechanical pump (PFEIFFER BALZERS, DUO 016 B) to a

base pressure of 10^{-2} mbar then flooded with N_2 at a flow rate of 40 ml/min for 10 min. Using a ramp rate of 40 °C/min, the furnace was ramped to the desired temperature held for 10 min, and then cooled naturally to room temperature. To determine the influence of selenization temperature on the properties of WSe_2 films, the precursors were selenized at temperatures of 350 °C, 400 °C, and 450 °C.

WSe_2 Films Characterization

To determine the thicknesses of WSe_2 films, an Alpha step IQ profilometer was used. Using a stylus force of 16.4 mg and a scan rate of 50 μm/s, the value of the thickness of each sample was determined. Phase identification was carried out using Bruker AXS D8 diffractometer system with a Cu Kα1 (λ = 1.540629 Å) radiation operated at 40 mA and 40 kV with Bragg-Brentano θ-2θ scanning mode. The crystalline phases were analyzed by comparing the measured Bragg diffraction peaks with the cards provided by the International Centre for Diffraction Data (ICDD) as ascribed by Mwakyusa et al. (2022). Using Williamson-Hall analysis, the value of the lattice macrostrain was estimated as described by Dubey et al. (2022). The surface morphology of the WSe_2 films was analyzed using a Veeco/Bruker Digital Instrument IIIa Multimode Atomic Force Microscopy (AFM). A model RTSESP7 silicon probe was used for tapping mode AFM scanning. The obtained images were further analyzed to determine the surface roughness, root mean surface, roughness, Maximum peak-to-valley height, skewness, and kurtosis of the WSe_2 films using Gwydion 2.53 software. Optical transmittance and reflectance were measured by using a UV-VIS-NIR double beam spectrophotometer (Perkin Elmer Lambda 1050^{+}) in the wavelength range $300\,nm \leq \lambda \leq 2500\,nm$ at room temperature. The reflection measurement was achieved at near normal (angle 5°) to the sample. The obtained information was used to estimate the absorption coefficient, bandgap and Urbach energy of the WSe_2 films. Using the Fresnel equation and optical reflectance data, the dependence of the optical constants on the selenization temperature for WSe_2 films was examined.

Results and discussion

The XRD measurement was first performed with the motivation of understanding the microstructure of the WSe_2 films. XRD patterns of WSe_2 films selenized at different temperatures are shown in Figure 1. A large number of sharp XRD peaks reveals the polycrystalline nature of the WSe_2 films. No peaks related to W were detected – indicating that all W metal phases reacted with Se to form WSe_2. However, XRD peaks related to W_5O_{14} were detected. This could be associated with the reaction of the films with ambient oxygen after selenization – as samples were shipped to Germany for the XRD analysis. As can be seen in Figure 1 (a), all the films are characterized by XRD peaks at $2\theta \approx 14.4°$ and $2\theta \approx 28.9°$, respectively corresponding to (002) and (004) of hexagonal WSe_2 (ICDD No.: 98-008-4181). The presence of these XRD peaks suggests that the *c*-axis of the WSe_2 films is normal to the substrate (*c*-axis substrate texture). This agrees with the findings reported by Genut et al. (1992). At temperatures of 350 °C and 450 °C, the XRD peaks of (102) were more prominent, along with weak peaks of (103) and (106) (as shown in Figure 1 with black and blue lines). This indicates a more random orientation of WSe_2 crystals at these temperatures. These observations are in good agreement with previous reports (Salitra et al 1994 and Hankare et al 2009). Interestingly, samples selenized at 400 °C showed strong (004) XRD peaks compared to (002) reflection, and very weak (103) and (106) peaks (see Figure 1 red line) revealing predominantly *c*-axis growth normal to the substrate. It has been documented that the presence of active oxygen-containing species strongly impacts the crystal orientations (Bertrand 1988). Looking at the XRD pattern of this sample, the peak related to W_5O_{14} is very weak, indicating the dominance of the WSe_2 phase.

As depicted in Figure 1, the XRD peaks associated with $(00l)$ – types of crystal orientations decrease with an increase in the selenization temperature. This suggests that

selenization temperature induces lattice strain in the WSe_2 films. Using Gauss fit, the Full Width at Half Maximum (FWHM) values of $(00l)$ – types of crystal orientations were evaluated (see Table 1). No peak shift for $(00l)$ – types XRD peaks have been observed. Interestingly, no significant difference for estimated and calculated FWHM and lattice strain for the XRD peak (002), respectively noticed. On the other hand, the XRD peak related to (004) demonstrated a remarkable difference in the FWHM and the lattice strain. The FWHM increased from 0.28° for the samples selenized at a temperature of 350 °C to 0.34° for samples selenized at 400 °C – further increase in temperature led to a decrease in the FWHM. The lattice strain of the samples selenized at a temperature of 350 °C was 0.28 and increased to 0.31 and remained constant at higher temperatures of 400 °C and 450 °C. It is worth noting that lattice strain can influence XRD peak broadening and lead to a decrease in the peak intensities. Based on this finding, it can be concluded that the selenization temperature strongly influences the lattice strain and $(00l)$ – types of crystal orientations.

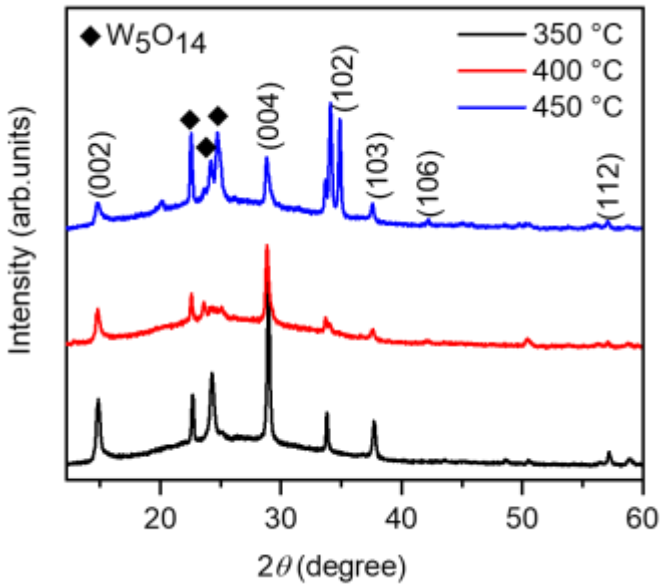

Figure 1: (a) XRD pattern of the WSe_2 films selenized at different temperatures

Table 1: The XRD parameters for $(00l)$ – types of crystal orientations of the WSe_2 films selenization at different temperatures obtained using

Selenization temperature (°C)	XRD peak (002)			XRD peak (004)		
	XRD peak position (°)	FWHM (°)	Lattice strain	XRD peak position (°)	FWHM (°)	Lattice Strain
350 °C	14.85	0.39	0.74	28.96	0.28	0.26
400 °C	14.82	0.38	0.74	28.87	0.34	0.31
450 °C	14.85	0.38	0.73	28.96	0.28	0.31

To have more conclusive information regarding the WSe_2 crystal orientation, the surface morphology of WSe_2 films selenized at different temperatures was studied. The

two-dimensional (2D) and the three-dimensional (3D), AFM micrographs of WSe_2 films selenized at different temperatures are displayed in Figure 2. As depicted in Figures 2 (a-1) and (a-2), samples selenized at 350 °C showed to have some grains that are completely parallel to the substrate (see Figure 2 (a-1) and (a-2) marked with a red circle). On the contrary, when selenization temperature increases to 400 °C most of the grains are perpendicular to the substrate (see Figure 2 (b-1) and (b-2)) – while higher selenization temperatures deteriorate the crystal orientation. This observation is in good agreement with the XRD data. A similar crystal orientation has been reported in the literature (Sierra-Castillo et al. 2020). Looking at the XRD pattern and AFM images (see Figures 1 and 2), it is possible to conclude that the crystal orientation depends on the amount of Se vapour in the reaction chamber (Han et al. 2019). For a selenization temperature of 350 °C the Se partial pressure in the reaction chamber is not higher enough to promote layer-by-layer growth. As the selenization temperature increases to 400 °C, the Se partial pressure is raised, provoking the layer-by-layer – thus, crystal orientation perpendicular to the *c*-axis is more visible. Considering the selenization temperature of 450 °C, most of the Se vapour escaped from the reaction chamber. As a result of this, Se partial pressure in the chamber decreases, hampering layer-by-layer growth.

Using statistical parameters such as average surface roughness, root mean square roughness, maximum peak-to-valley height, skewness, and kurtosis, the quantitative information on the influence of selenization temperature on the surface topography of WSe_2 films could be evaluated. The root mean square roughness measures the overall mean magnitude of surface variation, while the maximum peak-to-valley height gives the highest peak and lowest valley in the films – no significant variation between these two parameters was observed (see Table 1). As depicted in Table 1, a clear distinction in skewness and kurtosis was observed. All films exhibited positive skewness. This suggests that the samples are characterized by protruding narrow peaks with less deep valleys. However, samples selenized at 400 °C demonstrated relatively lower skewness values. A similar trend is visible for kurtosis data. Based on these findings, it can be concluded that height distribution for samples selenized at 400 °C is more symmetric. It can be concluded that the crystal orientation and peak-to-valley height distribution depend on the Se partial pressure during the selenization process. Following these observations, it can be concluded that the co-existence of different crystal orientations impacts the topographic properties of WSe_2 films. Further optimization of the film's growth this holds particularly to the Se partial pressure is expected to improve the film quality.

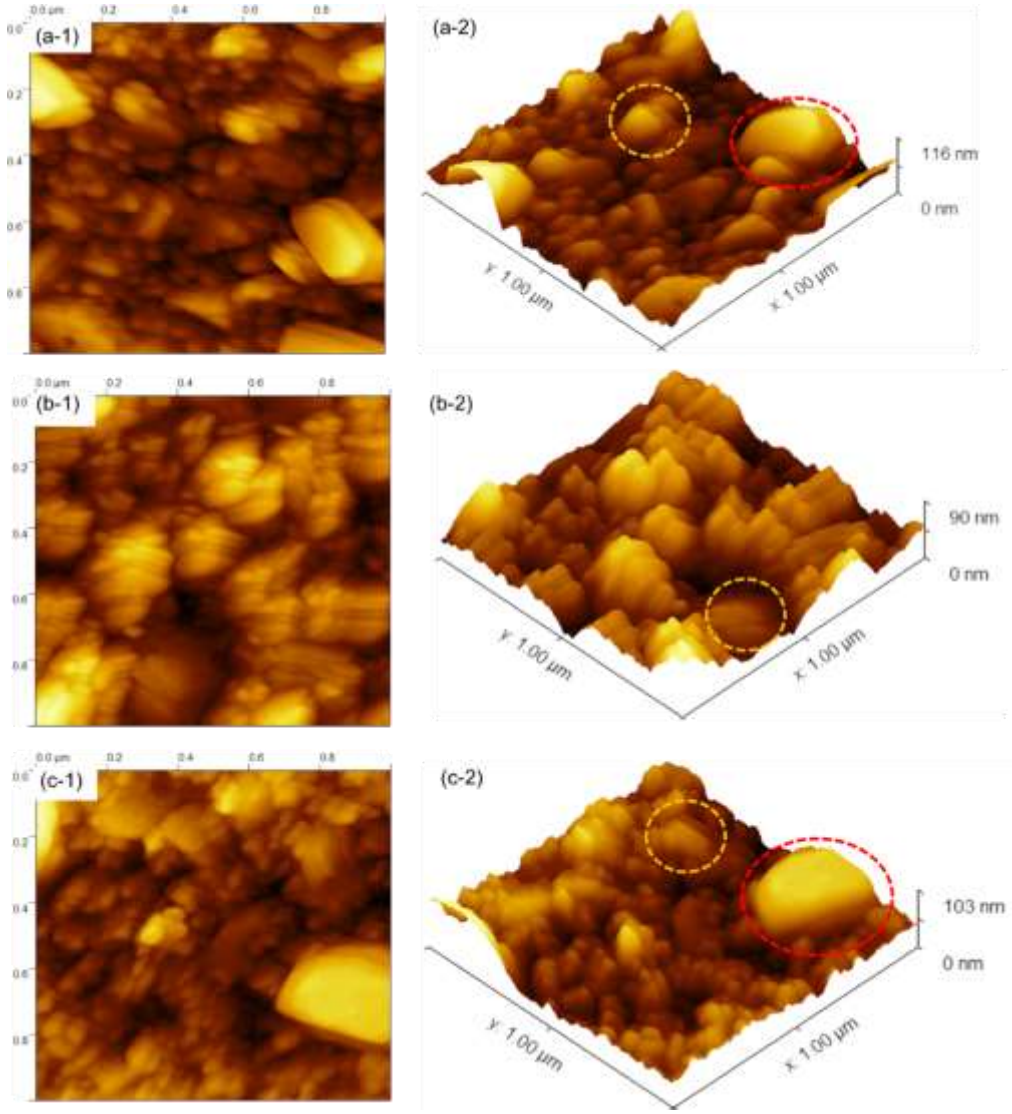

The diffraction diagrams

Figure 2: Tapping mode AFM topography of WSe_2 films selenized at 350 °C (2D (a-1) and 3D (a-2)), 400 °C (2D (b-1 and 3D (b-2)) and 450 °C (2D (c-1) and 3D (c-2))

Table 1: AFM parameters of the WSe_2 films selenized at different temperature

Selenization temperature (°C)	Average Roughness (nm)	Root Mean Square Roughness (nm)	Maximum Peak to Valley Height (nm)	Skewness	Kurtosis
350 °C	16.34	12.72	41.66	0.75	3.50
400 °C	10.40	12.74	40.80	0.20	2.80
450 °C	16.50	12.62	41.36	0.97	4.32

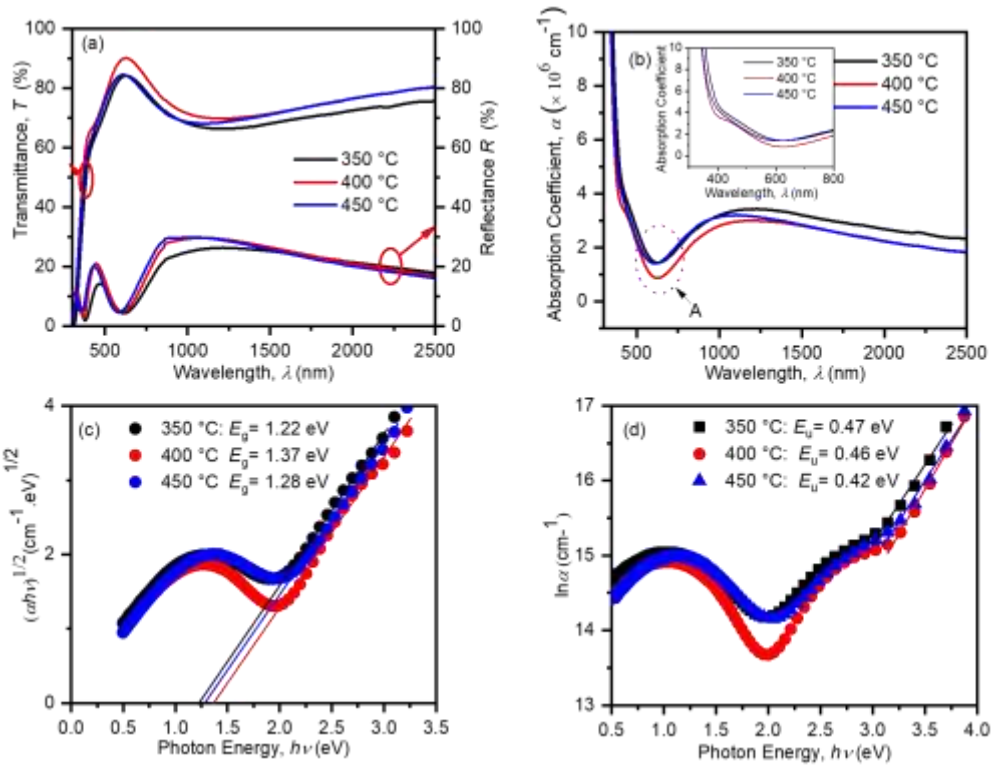

Figure 3: (a) the transmittance and reflectance spectra, (b) the dependence of absorption coefficient, (c) the Tauc plot, and (d) the $ln\alpha$ versus photon energy curves for WSe_2 films selenized at different temperatures.

To observe whether the selenization temperature affects the dielectric properties of WSe_2 films, the optical properties of the films were investigated. It is well known that the transmission and reflection behaviour of the materials gives good information about the electronic states and atomic vibration of those materials. Thus, the optical properties of WSe_2 films were investigated by looking at the UV-VIS-NIR transmission and reflectance properties of the films. The dependence of the optical transmittance of the WSe_2 films on selenization temperature is depicted in Figure 3 (a). It can be noted that all WSe_2 films demonstrated high optical transparency (above 85%) in the visible region. However, the sample selenized at 400 °C demonstrated the highest transparency. Based on these findings, it can be concluded that crystal orientations have an impact on the optical transparency of the films. Films with strong $(00l)$ - types of XRD peaks demonstrated higher optical transparency. Looking at reflectance spectra, all samples showed a reflectivity of below 20% in the visible spectrum which decreases after a wavelength of 1000 nm and then increases beyond a wavelength of 1500 nm (see Figure 3 (a)). This is in good agreement with transmittance spectra. These results demonstrate the potential of WSe_2 as a transparent window layer solar cell or a back contact in bifacial solar cells.

As shown in Figure 3 (b), the optical absorption patterns display strong optical absorption (labelled A) at the wavelength of 620 nm. This could be associated with excitonic absorption. An excitonic absorption in the range of 1.5 eV to 2.0 eV is attributed to the optical transition between a maximum valence band and a minimum conduction band at the K-point of the Brillouin zone (Han et al. 2019). This observation is in good agreement with previous reports (Salitra et al. 1994, Han

et al. 2019). As can be seen in Figure 3(b), as the selenization temperature increased from 350 °C to 400 °C, the absorption edge of the WSe_2 films shifted to the lower wavelengths, however, beyond 400 °C it reverted to the higher wavelengths (see an insert in Figure 3(b)). This could be associated with an increase or decrease in the bandgap of WSe_2 films. To further address this matter, the optical bandgap of WSe_2 films was estimated using Tauc's relation. It could be noted that the bandgap increases from 1.22 eV for samples selenized at 350 °C to 1.37 eV for samples selenized at 400 °C, then decreases beyond this temperature (see Figure 3 (c)). Our estimated values of bandgap are somewhat smaller compared to those reported in the literature (Han et al. 2019, Alzaid et al. 2022). A possible explanation for this observation is the presence of a few phases related to the W_5O_{14}. The existence of undesirable phases in materials has been proven as a potential factor in generating trap states with the bandgap that are expected to significantly reduce it. These observations and arguments are in good agreement with the observed XRD data (see Figure 1). The influence of defects on the quality of band edges of WSe_2 films was explored by analyses of the Urbach tail effect as ascribed by (Mwakyusa 2022). A linear fit of the plot of $ln\alpha$ versus photon energy yields a slope that could be used to evaluate Urbach energy, E_u. As can be seen in Figure 3(d), E_u slightly decreases with an increase in selenization temperature. It could be concluded that selenization has less effect on the Urbach energy of the WSe_2 films.

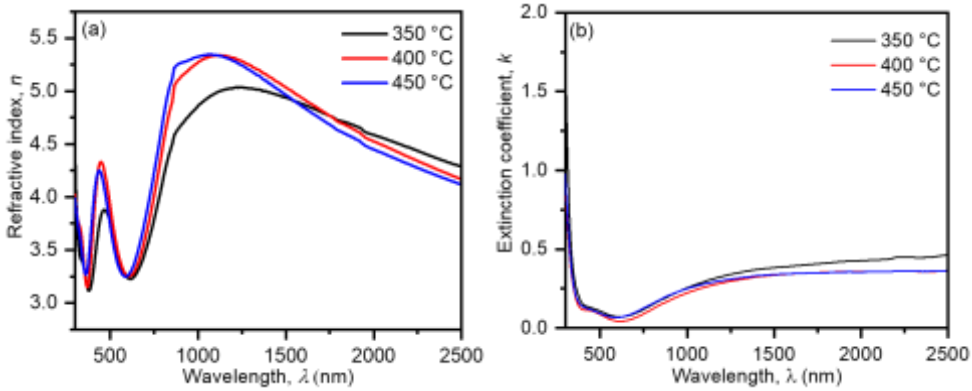

Figure 4: (a) Refractive index, *n*, and (b) extinction coefficient *k* as a function of wavelength for WSe_2 films selenized at different temperatures.

The refractive index and extinction coefficient of semiconductors are paramount important when designing optoelectronic devices. The dependence of the refractive index and extinction coefficient of WSe_2 films on the selenization temperature required a detailed understanding. In line with this argument, the optical refraction data was used to estimate the values of the refractive index as described by Sharma et al. (2015). On the other hand, the obtained values of the absorption coefficient were utilized to determine the extinction coefficient of the films. It can be seen from the graph (see Figure 4(a)) that the refractive index somewhat increases as the annealing temperature increases. It is well acknowledged that high selenization temperatures tend to promote the formation of larger grains and improved crystallinity. This is expected to increase the refractive index of the films. Looking at the extinction coefficient, no significant difference was noticed (see Figure 4 (b)).

Conclusion

WSe_2 films were prepared by selenization of DC-sputtered W metal precursors. The influence of selenization temperature on the structural, morphology, and optical properties of WSe_2 films has been investigated. The crystallographic analysis showed the co-

existence of perpendicular and parallel substrate texture. The AFM studies revealed the nanocrystalline nature of WSe_2 films which are characterized by protruding narrow peaks with less deep valleys. However, more superior crystal orientation (perpendicular substrate texture) and morphology were obtained for a selenization temperature of 400 °C. The optical transmission spectra showed higher transparency of above 85% in the visible region – favouring the applicability of the materials as a back contact for bifacial solar cells. Further, the optical studies showed a strong absorption peak A at 620 nm – due to excitonic absorption features. The estimated bandgap increases from 1.22 eV to 1.37 eV when the selenization temperature increases from 350 °C to 400 °C – while higher selenization temperatures reduce the bandgap, mainly due to the presence of W_5O_{14} phases. It was further found that the Urbach energy does not strongly depend on the selenization temperature. The refractive index somewhat increases with an increase in selenization temperature.

Author Contributions

The scientific idea, laboratory work and manuscript writing were done by the author.

Declaration of conflict of interest

The authors declare no competing financial interest.

Acknowledgement

The author gratefully acknowledges the International Science Program (ISP) of Uppsala University, Sweden, and the Materials Science and Solar Energy Network for Eastern and Southern Africa (MSSEESA) for research materials and facilities. Furthermore, Mr. Elisante Maloda is highly acknowledged for XRD measurement.

Reference

Alzaid M, Hadia NMA, Shaaban ER, Hagary ME, Mohamed WS 2022 Thickness controlling bandgap energy, refractive index and electrical conduction mechanism of 2D Tungsten Diselenide (WSe_2) thin films for photovoltaic applications. *Appl. Phys. A* 128 (94): 790. https://doi.org/10.1007/s00339-021-05188-z

Bett AJ, Winkler KM, Bivour M, Cojocaru L, Kabakli ÖŞ, Schulze PSC, Siefer G, Tutsch L, Hermle M, Glunz SW, Goldschmidt JC 2019 Semi-Transparent Perovskite Solar Cells with ITO Directly Sputtered on Spiro-OMeTAD for Tandem Applications. *ACS Appl. Mater. Interfaces* 11(49): 45796–45804. https://doi.org/10.1021/acsami.9b17241.

Bertrand PA 1988 Orientation of rf-sputter-deposited MoS_2 films. *J. Mate.r Res.* 4(1): 180-184 https://doi.org/10.1557/JMR.1989.0180.

Bin Rafiq MKS, Amin N, Alharbi HF Luqman M, Ayob A, Alharthi SY, Alharthi HN, Bais B and Akhtaruzzaman M 2020 WS_2: A New Window Layer Material for Solar Cell Application. Sci. Rep.10: 771. https://doi.org/10.1038/s41598-020-57596-5

Bozheyev F, Friedrich D, Nie M, Rengachari M, and Ellmer K 2017 Highly (001)-textured *p*-type WSe_2 Thin Films as Efficient Large-Area Photocathodes for Solar Hydrogen Evolution *Sci. Rep.* 7: 16003 https://doi.org/10.1038/s41598-017-16283-8

Brent RJ, Savjani N, O'Brien P 2017 Synthetic approaches to two-dimensional transition metal dichalcogenide nanosheets. *Prog. Mater. Sci.* 89: 411-478. https://doi.org/10.1016/j.pmatsci.2017.06.002.

Cheng Q, Pang J, Sun D, Wang J, Zhang S, Liu F, Chen Y, Yang R, Liang N, Lu X, Ji Y, Wang J, Zhang C, Sang Y, Liu H, Zhou W 2020 WSe_2 2D *p*-type semiconductor-based electronic devices for information technology: Design, preparation, and applications. InfoMat 2(4): 656-697. https://doi.org/10.1002/inf2.12093.

Dubey K, Zaidi A, Awasthi R 2022 Environmentally Benign Structural, Topographic, and Sensing Properties of Pure and Al-doped ZnO Thin Films. *ACS Omega* 7(33) 28946 – 28954 https://doi.10.1021/acsomega.2c02440.

Gautam S, Patel AK, Mishra R and Mishra O 2022 Performance analysis of WSe_2 solar cell with Cu_2O hole transport layer by optimization of electrical and optical properties. *J. Comput. Electron*. 21, 1373–1385. https://doi.org/10.1007/s10825-022-01941-6.

Genut M, Margulis L, Tenne R, Hodes G 1992 Effect of substrate on growth of WS_2 thin films. *Thin Solid Films* 219 (1-2): 30-36. https://doi.org/10.1016/0040-6090(92)90720-V.

Han A, Aljarb A, Liu S, Li P, Ma C, Xue F, Lopatin S, Yang C-W, Huang J-K, Wan Y, Zhang X, Xiong Q, Huang K-W, Tung V, Anthopoulos TD, Li L-J 2019 Growth of 2H stacked WSe_2 bilayers on sapphire. *Nanoscale Horiz*. 4: 1434-1442. https://doi.org/10.1039/C9NH00260J.

Hankare PP, Manikshete AH, Sathe DJ, Chate PA, Patil AA, Garadkar KM 2009 A novel route of synthesis of WS_2 thin film and its characterization. *J Cry Growth* 311 (13): 3386-3388. https://doi.org/10.1016/j.jcrysgro.2009.04.012.

Haque D, Ali H, Islam ZA 2021 Efficiency enhancement of WSe_2 heterojunction solar cell with CuSCN as a transport layer: A numerical simulation approach. *Sol Energy* 230 528-537. https://doi.org/10.1016/j.solener.2021.10.054.

Kadiwala K, Butanovs E, Ogurcovs A, Zubkins M and Polyakov B 2022 Comparative study of WSe_2 thin films synthesized via pre-deposited WO_3 and W precursor material selenization. *J Cryst Growth* 593: 126764. https://doi.org/10.1016/j.jcrysgro.2022.126764.

Lin Y, Bersch B, Addou R, Xu K, Wang Q, Smyth C, Jariwala B, Walker R, Fullerton-Shirey S, Kim M, Wallace R, Robinson J 2020 Modification of the Electronic Transport in Atomically Thin WSe_2 by Oxidation. Adv. Mater. Interfaces 7(18): 2000422. https://doi.org/10.1002/admi.202000422.

Mao X, Zou J, Li H, Song Z, He S 2018 Magnetron sputtering fabrication and photoelectric properties of WSe_2 film solar cell device. *Appl Surf Sci* 444: 126-132. https://doi.org/10.1016/j.apsusc.2018.02.249

Morrish R, Haak T, and Colin A 2014 Low-Temperature Synthesis of *n*-Type WS_2 Thin Films via H_2S Plasma Sulfurization of WO_3 *Chem. Mater* 26 (13): 3986-3992. https://doi: 10.1021/cm501566h.

Mwakyusa LP 2022 Properties of (Cd, Zn)S films deposited by DC co-sputtering. *Tanz J Engrg Technol* 41 (4): 150-156. https://doi.org/10.52339/tjet.v41i4.799.

Mwakyusa LP, Mlyuka NR and Samiji ME 2022 Boron Doped ZnO Films Deposited by DC Reactive Sputtering Using Zn:B Target: Influence of the Deposition Temperature on the Structural, Electrical and Optical Properties. *Tanz J Sci* 48 (1): 148-155. https://dx.doi.org/10.4314/tjs.v48i1.14.

Rahman MA 2022 Performance analysis of WSe_2-based bifacial solar cells with different electron transport and hole transport materials by SCAPS-1D. *Heliyon* 8(6): e09800. https://doi.org/10.1016/j.heliyon.2022.e09800.

Salitra G, Hodes G, Klein E, Klein E 1994 Highly oriented WSe_2 thin films prepared by selenization of evaporated WO_3. *Thin Solid Films* 245 (1-2): 180-185. https://doi.org/10.1016/0040-6090(94)90896-6.

Sharma S, Pariasamy C, Chakrabarti P 2015 Thickness Dependent Study of RF Sputtered ZnO Thin Films for Optoelectronic Device Application. *Electron Mater Lett* 11(6): 1093-1101. https://10.1007/s13391-015-4445-y.

Sierra-Castillo A, Haye E, Acosta S, Bittencourt C, Colomer J-F 2020 Synthesis and Characterization of Highly Crystalline Vertically Aligned WSe_2 Nanosheets. *Appl. Sci.* 10: 874. https://doi.org/10.3390/app10030874

Villamayor MMS, Lindblad A, Johansson FOL, Tran T. Pham NH, Primetzhofer D, Sorgenfrei NLAN, Giangrisotomi E, Föhlisch A, Lourenço P, Bernard R,

Witkowski N, Prévot G, Nyberg T 2021 Growth of two-dimensional WS_2 thin films by reactive sputtering. *Vacuum* 188: 110205. https://doi.org/10.1016/j.vacuum.2021.110205.

Zhang X, Teng SY, Loy ACM, How BS, Leong WD, Tao X 2020a. Transition Metal Dichalcogenides for the Application of Pollution Reduction: A Review. *Nanomaterials* 10(6): 1012. https://doi:10.3390/nano10061012.

Zhang X, Yao B, Li Y, Ding Z, Zhao H, Zhang L, Zhang Z 2020b Influence of WSe_2 buffer layer at back electrode on performance of $Cu_2ZnSn(S,Se)_4$ solar cells. *Sol Energy* 199: 128-135. https://doi.org/10.1016/j.solener.2020.02.033.